



Cite this: *Dalton Trans.*, 2018, **47**, 1958

A helical chain-like organic–inorganic hybrid arsenotungstate with color-tunable photoluminescence†

Hechen Wu, Rong Wan, Yanan Si, Pengtao Ma,* Jingping Wang  and Jinyang Niu *

A 1-D infinite helical chain-like organic–inorganic hybrid arsenotungstate $\text{Na}_4\text{H}_6\{[\text{Pr}(\text{H}_2\text{O})_2]_2\{\text{As}_2\text{W}_{19}\text{O}_{68}\}(\text{WO}_2(\text{mal}))_2\}_2\cdot 24\text{H}_2\text{O}$ (mal = malate) (**1**) was prepared, which was characterized by elemental analyses, thermogravimetric (TG) analyses, IR spectroscopy, powder X-ray diffraction (PXRD) and X-ray single-crystal diffraction. Structural characterization revealed that **1** comprises the organo-functionalized $[\{\text{As}_2\text{W}_{19}\text{O}_{68}\}(\text{WO}_2(\text{mal}))_2]^{18-}$ polyanions hinged together by the Pr^{3+} ions forming a 1-D infinite helical chain-like architecture. The malate ligand may play a vital role to stabilize the structure of **1** by the formation of the five-membered W–O–C–C–O chelate ring. Solid state photoluminescence reveals that **1** features excitation wavelength-dependent emission properties, achieving a reversible emission color switching simply *via* changing the excitation wavelength. Time-resolved emission spectroscopy (TRES) indicates that the photoexcitation $\text{O} \rightarrow \text{M}$ ligand to metal charge transfer (LMCT) of arsenotungstate fragments can sensitize the Pr^{3+} ions through intramolecular energy transitions in **1**.

Received 6th December 2017,
Accepted 2nd January 2018

DOI: 10.1039/c7dt04608a

rsc.li/dalton

Introduction

The photoluminescence (PL) behaviors of lanthanides (Ln) have generated great interest over several decades owing to their extensive applications in light-emitting diodes, lighting and displays, and biomedical drugs.¹ Ln^{3+} ions are widely used in optical applications that originate from the unique $4f^n$ electronic configuration generating a large variety of electronic levels.² However, Ln^{3+} ions possess an intrinsically low molar absorptivity because of the forbidden f–f transitions, and the agent is required to participate in energy absorption and energy transfer to sensitize Ln^{3+} ions *via* an antenna effect. Fortunately, Ln^{3+} ions can be also described as good electron acceptors because of a series of unoccupied 5d or 6s orbitals to accept lone pair electrons from organic or inorganic ligands forming covalent bonds.³ Polyoxometalates (POMs) are composed of MO_x (M = Mo, W, V, Nb or Ta) polyhedra fused

together in an edge-, a corner- or a face-shared fashion, sometimes along with the insertion of heteroatoms. The unmatched structural diversity and oxygen-rich surface of POMs aid in the construction of abundant POM-based complexes by acting as outstanding inorganic ligands.⁴ The Ln-based POM (Ln-POM) complexes may extensively expand the physical and chemical properties of both components.⁵ In Ln-POM complexes, the $\text{O} \rightarrow \text{M}$ ligand to metal charge transfer (LMCT) of POM can sensitize the luminescence of Ln^{3+} ions through intramolecular energy transitions. In addition, the reported Ln-POMs have displayed a series of catalysis, medicinal, nanotechnology and magnetic properties.⁶ Thus, increasing interest has been focused on the formation of Ln-POMs, and plenty of Ln-POMs have been isolated to date. Since Peacock and Weakley reported the first Ln-substituted polyoxotungstates (POTs) $[\text{LnW}_{10}\text{O}_{36}]^{9-}$ (Ln = La^{3+} , Ce^{3+} , Pr^{3+} , Nd^{3+} , Sm^{3+} , Ho^{3+} , Er^{3+} , Yb^{3+} , and Y^{3+}) and $[\text{LnW}_{10}\text{O}_{36}]^{8-}$ (Ln = Ce^{4+}) in 1971,⁷ a myriad of unexpected Ln-POTs emerged one after another over the next several decades. Until now, most of the reported Ln-POT complexes were discrete oligomers, yet 1-D chain-like Ln-POT structures were relatively less addressed (Table S1†). In 2000, Pope and coworkers first isolated two 1-D infinite zigzag chain-like Ln-POTs $[\text{La}(\alpha\text{-SiW}_{11}\text{O}_{39})(\text{H}_2\text{O})_3]^{5-}$ and $[\text{Ce}(\alpha\text{-SiW}_{11}\text{O}_{39})(\text{H}_2\text{O})_3]^{5-}$ based on monolacunary POT $[\alpha\text{-SiW}_{11}\text{O}_{39}]^{8-}$.⁸ Inspired by this fascinating work, Mialane *et al.* separated two phosphotungstate based $[(\alpha\text{-PW}_{11}\text{O}_{39})]^{8-}$ subunits $[\text{Eu}(\alpha\text{-PW}_{11}\text{O}_{39})(\text{H}_2\text{O})_2]^{5-}$ (1-D infinite zigzag chain arrangement)

Henan Key Laboratory of Polyoxometalate Chemistry, Institute of Molecular and Crystal Engineering, College of Chemistry and Chemical Engineering, Henan University, Kaifeng, Henan 475004, P. R. China. E-mail: mpt@henu.edu.cn, jymiu@henu.edu.cn; Fax: +86-371-23886876

† Electronic supplementary information (ESI) available: Survey of already synthesized 1-D chain Ln-POTs, PXRD and TGA results, the decay time diagram of **1** under different emission wavelengths, the front and top views of the 3D surface plot of the luminescence photoexcitation map of **1**, and the 2D diagram of the luminescence photoexcitation map of **1**. CCDC 1588091. For ESI and crystallographic data in CIF or other electronic format see DOI: 10.1039/c7dt04608a

and $[\text{Yb}(\alpha\text{-PW}_{11}\text{O}_{39})(\text{H}_2\text{O})_2]^{5-}$ (1-D infinite linear chain arrangement) in 2003.⁹ Three years later, Luo *et al.* synthesized a 1-D helical chain-like Ln-POT $[\text{Ce}(\text{H}_2\text{O})(\text{DMF})_6(\text{W}_{10}\text{O}_{32})]\cdot\text{DMF}\cdot\text{CH}_3\text{CH}_2\text{OH}$ (DMF = dimethyl formamide) by assembly of decatungstate $[\text{W}_{10}\text{O}_{32}]^{4-}$ and $[\text{Ce}(\text{H}_2\text{O})(\text{DMF})_6]^{4+}$ fragments under mild conditions.¹⁰ In the same year, Wang *et al.* reported a 1-D infinite extended architecture $[\text{Nd}_3(\text{H}_2\text{O})_{17}(\alpha\text{-P}_2\text{W}_{17}\text{O}_{61})]^-$ built of $[\{\text{Nd}(\text{H}_2\text{O})_7\}_2\{\text{Nd}(\text{H}_2\text{O})_3(\alpha\text{-P}_2\text{W}_{17}\text{O}_{61})_2\}_2]^{8-}$ fragments and Nd^{3+} ions.¹¹ In 2009, Kortz *et al.* obtained two Ln-POTs $[\text{Ln}_2(\text{H}_2\text{O})_{10}\text{W}_{22}\text{O}_{72}(\text{OH})_2]^{8-}$ (Ln = La^{3+} and Ce^{3+}), in which the $[\text{H}_2\text{W}_{22}\text{O}_{74}]^{14-}$ polyanions as tridentate ligands joined together by two Ln^{3+} ions constructing a 1-D chain structure.¹² The next, Boskovic and coworkers obtained two 1-D chain-like arsenotungstates $[\text{Nd}_3\text{As}_4\text{W}_{41}\text{O}_{141}\text{OH}(\text{H}_2\text{O})_{10}]^{16-}$ and $[\text{Dy}_4\text{As}_2\text{W}_{22}\text{O}_{76}(\text{H}_2\text{O})_{19}(\text{C}_2\text{H}_5\text{NO}_2)_2]^{2-}$ by the reaction of the $[\text{As}_2\text{W}_{19}\text{O}_{67}(\text{H}_2\text{O})]^{14-}$ precursor and Nd^{3+} or Dy^{3+} ions in acidic aqueous solutions (pH < 2).¹³ Since 2004, our group has been exploring the design and synthesis of Ln-POTs, and have prepared a series of 1-D chain-like Ln-POT materials. In 2004, our group synthesized a 1-D chain-like silicotungstate $[(\text{Pr}(\text{H}_2\text{O})_4\text{SiW}_{11}\text{O}_{39})(\text{NaPr}_2(\text{H}_2\text{O})_{12})(\text{Pr}(\text{H}_2\text{O})_4\text{SiW}_{11}\text{O}_{39})]^{3-}$.¹⁴ Two years later, we reported two 1-D zigzag chain-like Ln-POTs $[\text{Nd}_{1.50}(\text{GeW}_{11}\text{O}_{39})(\text{H}_2\text{O})_6]^{3.5-}$ and $[\text{Sm}_{1.25}(\text{GeW}_{11}\text{O}_{39})(\text{H}_2\text{O})_4]^{4.25-}$,¹⁵ concurrently, we also separated two organic-inorganic hybrid 1-D chain-like Ln-POTs $[\text{Sm}(\text{H}_2\text{O})_6]_{0.25}[\text{Sm}(\text{H}_2\text{O})_5]_{0.25}\text{H}_{0.5}\{\text{Sm}(\text{H}_2\text{O})_7[\text{Sm}(\text{H}_2\text{O})_2(\text{DMSO})(\alpha\text{-SiW}_{11}\text{O}_{39})]\cdot 4.5\text{H}_2\text{O}$ and $[\text{Dy}(\text{H}_2\text{O})_4]_{0.25}[\text{Dy}(\text{H}_2\text{O})_6]_{0.25}\text{H}_{0.5}\{\text{Dy}(\text{H}_2\text{O})_7[\text{Dy}(\text{H}_2\text{O})_2(\text{DMSO})(\alpha\text{-GeW}_{11}\text{O}_{39})]\cdot 5.25\text{H}_2\text{O}$ (DMSO = dimethyl sulfoxide).¹⁶ Afterwards, we obtained a Tm-substituted Keggin-type phosphotungstate $[(\alpha\text{-PW}_{10}\text{O}_{38})\text{Tm}_2(\text{C}_2\text{O}_4)(\text{H}_2\text{O})_2]^{3-}$ with a 1-D chain architecture based on the infrequent divacant $[\alpha\text{-x-PW}_{10}\text{O}_{38}]^{11-}$ polyanion.¹⁷ In 2015, our group obtained a 1-D linear chain-like Tb-substituted POT $[\text{Tb}(\text{H}_2\text{O})_2(\alpha\text{-PW}_{11}\text{O}_{39})]^{4-}$, in which Tb^{3+} ions act as linkers to bridge two adjacent monolacunary $[\alpha\text{-PW}_{11}\text{O}_{39}]^{7-}$ polyanions to construct a 1-D chain architecture.¹⁸ Besides, several 1-D chain-like coordination polymers with giant $\{\text{Mo}_{36}\}$ polymolybdates $[\{\text{Ln}(\text{H}_2\text{O})_6\}_2\{\text{Ln}(\text{H}_2\text{O})_7\}_2\{\text{Mo}_{36}(\text{NO})_4\text{O}_{108}(\text{H}_2\text{O})_{16}\}_n\cdot n\text{H}_2\text{O}$ [Ln = La, $n = 29$; Ln = Ce, $n = 41$; Ln = Pr, $n = 40$; Ln = Nd, $n = 36$] were reported by Fedin *et al.*¹⁹

It is very apparent that most mentioned 1-D Ln-POMs are purely inorganic, and the investigations on organic-inorganic hybrid 1-D chain-like Ln-POMs are relatively rare. Recently we have successfully synthesized an organic-inorganic hybrid 1-D helical chain-like Ln-POT $\text{Na}_4\text{H}_8\{\{\text{Pr}(\text{H}_2\text{O})_2\}_2\{\text{As}_2\text{W}_{19}\text{O}_{68}\}\{\text{WO}_2(\text{mal})\}_2\}\cdot 24\text{H}_2\text{O}$ (mal = malate) (**1**). **1** comprises the organo-functionalized $[\{\text{As}_2\text{W}_{19}\text{O}_{68}\}\{\text{WO}_2(\text{mal})\}_2]^{18-}$ polyanions hinged together by the Pr^{3+} ions forming a 1-D infinite helical chain-like structure. The malate ligand may play an important role to stabilize the structure of **1** by the formation of the five-membered W-O-C-C-O chelate ring. The PL study showed here that **1** features excitation wavelength-dependent emission properties. Through time-resolved emission spectroscopy (TRES), we found that the photoexcitation O → M ligand to metal charge transfer (LMCT) of arsenotungstate fragments can sensitize the Pr^{3+} ions through intramolecular energy transitions in **1**.

Results and discussion

Crystal structure

The existence of diffraction peaks in the experimental PXRD patterns of **1** is consistent with those of simulated PXRD patterns from the single-crystal X-ray diffraction, indicating the good phase purity for **1** (Fig. S1†).

1 was synthesized by the reaction of a dilacunary $[\text{As}_2\text{W}_{19}\text{O}_{67}(\text{H}_2\text{O})]^{14-}$ precursor with $\text{PrCl}_3\cdot 6\text{H}_2\text{O}$ and L-malic acid under mild conditions. As a kind of versatile precursor, $[\text{As}_2\text{W}_{19}\text{O}_{67}(\text{H}_2\text{O})]^{14-}$ can be described as two trivalent Keggin-type $\{\text{B}\text{-}\alpha\text{-AsW}_9\text{O}_{33}\}$ subunits linked by an additional $\{\text{WO}(\text{H}_2\text{O})\}$ group (Fig. 1a). Moreover, the $[\text{As}_2\text{W}_{19}\text{O}_{67}(\text{H}_2\text{O})]^{14-}$ precursor can easily fragment to provide arsenotungstate cluster subunits or tungstate-oxo fragments for the assembly of new structural architectures in aqueous solution.²⁰ Notably, the central moiety changes from *trans*- $\text{WO}(\text{H}_2\text{O})^{4+}$ to *cis*- $\text{WO}(\text{H}_2\text{O})^{4+}$ on going from $[\text{As}_2\text{W}_{19}\text{O}_{67}(\text{H}_2\text{O})]^{14-}$ precursor to **1**, opening up the As...O...As angle in the product. As a result, the As-As distance of 7.589(17) Å in **1** (Fig. 1b) is obviously longer than that of 6.334(11) Å in the $[\text{As}_2\text{W}_{19}\text{O}_{67}(\text{H}_2\text{O})]^{14-}$ precursor (Fig. 1a), and a larger angle of As-W($\{\text{WO}(\text{H}_2\text{O})\}$)-As (160.04(10)°) (Fig. 1b) is observed compared to the angle of 110.01(5)° in the $[\text{As}_2\text{W}_{19}\text{O}_{67}(\text{H}_2\text{O})]^{14-}$ precursor (Fig. 1a).

Single-crystal X-ray analysis revealed that **1** crystallizes in the monoclinic space group $C2/c$ (Fig. 1c), which is comprised of one $[\{\text{As}_2\text{W}_{19}\text{O}_{68}\}\{\text{WO}_2(\text{mal})\}_2]^{18-}$ arsenotungstate polyanion, two $[\text{Pr}(\text{H}_2\text{O})_2]^{3+}$ moieties, four Na^+ cations and twenty-four lattice water molecules, and eight protons for the charge balance of the polyanion. Bound into the vacant site of $[\{\text{As}_2\text{W}_{19}\text{O}_{68}\}\{\text{WO}_2(\text{mal})\}_2]^{18-}$ polyanions are two symmetric eight-coordinate Pr centers (Fig. 1d), which display a distorted square antiprismatic configuration with the Pr-O distances in the range of 2.353(5)–2.532(5) Å. The square antiprismatic geometry is achieved by five terminal oxygen atoms O18, O20, O23, O10A (symmetry code: A = 2 - x, y, 0.5 - z) and O11A from the $[\{\text{As}_2\text{W}_{19}\text{O}_{68}\}\{\text{WO}_2(\text{mal})\}_2]^{18-}$ polyanion with the Pr-O distances in the range of 2.353(5)–2.464(5) Å, one terminal oxygen atom O7B (symmetry code: B = 1.5 - x, 0.5 - y, -z) from another adjacent $[\{\text{As}_2\text{W}_{19}\text{O}_{68}\}\{\text{WO}_2(\text{mal})\}_2]^{18-}$ polyanion with the Pr-O7B distance of 2.431(5) Å, and two water ligands (O1 W and O2 W) with the Pr-O(W) distances in the range of 2.515(5)–2.532(5) Å. The two bottom planes for the Pr centre are defined by the oxygen atoms O18, O20, O23, O11A and O1 W, O2 W, O10A, O7B with the average deviations of least-squares planes of 0.066 and 0.244 Å. The dihedral angle for the two bottom square planes is 1.70°, and the distances between the Pr centre and two bottom planes are 1.294 and 1.374 Å, respectively. In **1**, the distances of the W-O bond are in the range of 1.682(6)–2.426(6) Å, and the angles of the O-W-O bond range from 70.9(2) to 172.3(3)°. All of the above indicate that the square antiprismatic configuration is distorted, which may be attributed to different coordination environments as a result of different coordination atoms. Meanwhile, the malate coordinates with the W11 atom through O37 (from

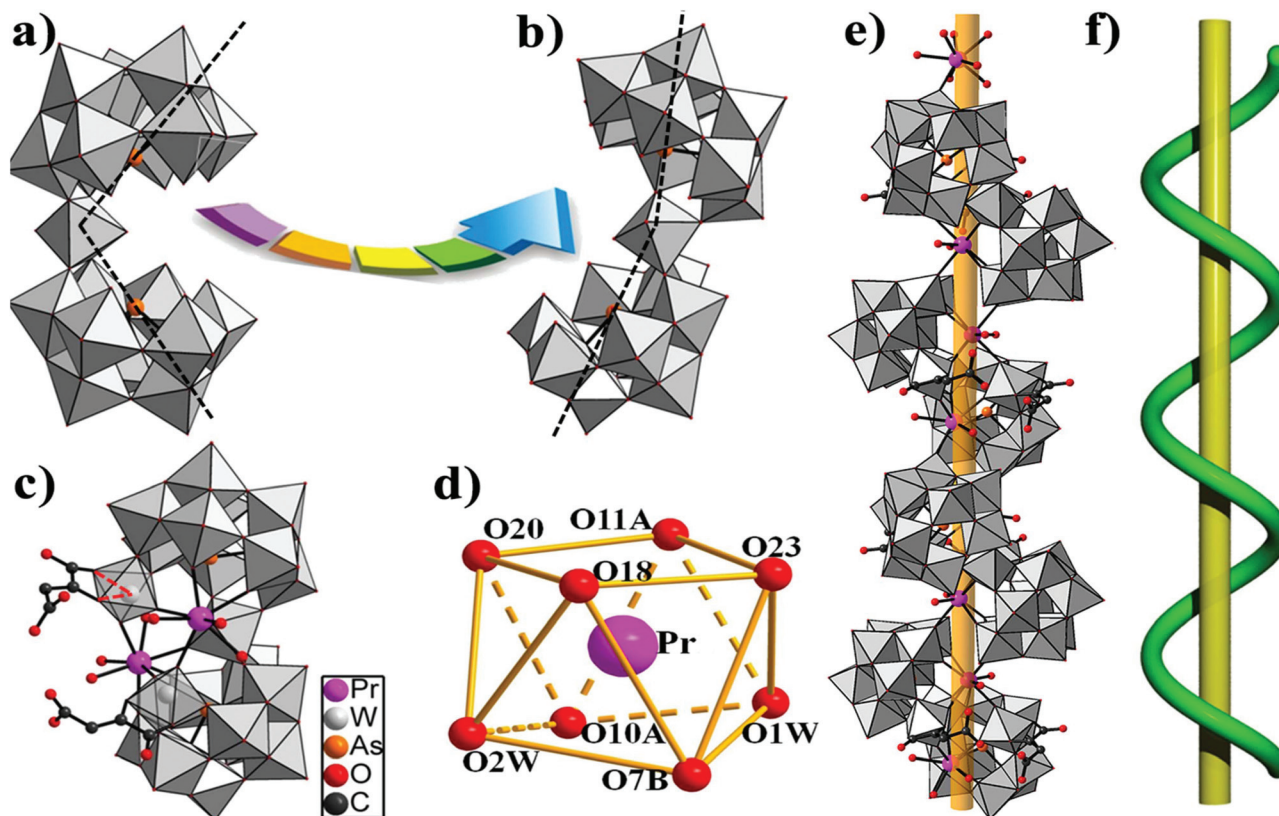


Fig. 1 (a) The polyhedron representation of the precursor $[\text{As}_2\text{W}_{19}\text{O}_{67}(\text{H}_2\text{O})]^{14-}$. (b) The polyhedron representation of the variable $\{\text{As}_2\text{W}_{19}\}$ unit in **1**. (c) The polyhedron representation of the polyanion unit of **1**. (d) The coordination environment of the Pr ion in **1**. The atoms with "A" in their labels are symmetrically generated (A: $2 - x, y, 0.5 - z$). The atoms with "B" in their labels are symmetrically generated (B: $1.5 - x, 0.5 - y, -z$). (e) The helical chain structure of **1**. (f) The model of single helical chain. K^+ cations and dissociative water molecules were omitted for clarity.

the carboxyl group) and O39 (from the hydroxyl group) to construct a five-membered W–O–C–C–O ring (Fig. S2[†]), thereby the malate ligand may play a constructive role to stabilize the structure of **1** by the formation of a five-membered chelate ring.

In addition, adjacent $[\{\text{As}_2\text{W}_{19}\text{O}_{68}\}\{\text{WO}_2(\text{mal})\}_2]^{18-}$ polyanions are bridged by Pr^{3+} ions, giving rise to a 1-D helical chain with a screw pitch of 23.89(1) Å (Fig. 1e). As we know, the helical structures are ubiquitous in nature and are basic architectures of the genetic code. Luo *et al.* reported a 1-D helical chain architecture $[\text{Ce}(\text{H}_2\text{O})(\text{DMF})_6(\text{W}_{10}\text{O}_{32})] \cdot \text{DMF} \cdot \text{CH}_3\text{CH}_2\text{OH}$ based on decatungstate, and rare quadrivalent cerium complex fragment $\{\text{Ce}(\text{H}_2\text{O})(\text{DMF})_6\}$ building blocks are bound to $[\text{W}_{10}\text{O}_{32}]^{4-}$ fragments through two corner-sharing bridging oxygen atoms from two adjacent $[\text{W}_{10}\text{O}_{32}]^{4-}$ to construct the helical chain (Fig. S3[†]).¹⁰ Recently, Cronin and coworkers have reported a double-helix POM $\text{Na}_2[(\text{HGMP})_2\text{Mo}_5\text{O}_{15}] \cdot 7\text{H}_2\text{O}$, whose helical parameters, such as rise per turn and helical twist per dimer, are closely identical to the left-hand Z-form of DNA, and it would be a great milestone in the development of the POM-based biochemistry.²¹ In this article, the single-helix structure of **1** has a close resemblance to that of the single-stranded RNA helix.

IR spectra

The IR spectra of **1**, $\text{K}_{14}[\text{As}_2\text{W}_{19}\text{O}_{67}(\text{H}_2\text{O})]$ precursor and L-malic acid have been recorded in KBr pellets on a Bruker VERTEX 70 IR spectrometer in the region of 400–4000 cm^{-1} . As shown in Fig. 2, four signals of characteristic vibration absorption bands appear at 952, 858, 790, and 710 cm^{-1} for **1**, which are assigned to the stretching vibrations $\nu(\text{W}-\text{O}_i)$, $\nu(\text{W}-\text{O}_b-\text{W})$, $\nu(\text{As}-\text{O}_a)$ and $\nu(\text{W}-\text{O}_c-\text{As})$, respectively. The signals of the L-malic acid at 1733 and 1401 cm^{-1} are assigned to the asymmetric stretching vibration $\nu_{\text{as}}(\text{COO}^-)$ and symmetric stretching vibration $\nu_{\text{s}}(\text{COO}^-)$, whereas the asymmetric stretching vibration appearing at 1633 cm^{-1} with the red shift of about 100 cm^{-1} is due to the coordination effect of the malate ligand and W atom in **1**. It should be noticed that the asymmetric stretching vibration $\nu_{\text{as}}(\text{COO}^-)$ obviously overlaps with the $\nu(\text{O}-\text{H})$ bending mode of lattice water in **1**. All the results indicate the presence of the $\text{K}_{14}[\text{As}_2\text{W}_{19}\text{O}_{67}(\text{H}_2\text{O})]$ precursor and malate in **1** that match well with the recorded data from single-crystal X-ray diffraction.

Photoluminescence properties

In 1931, Commission Internationale de l'Eclairage (CIE) recommended three primary colors red, green and blue (X, Y and

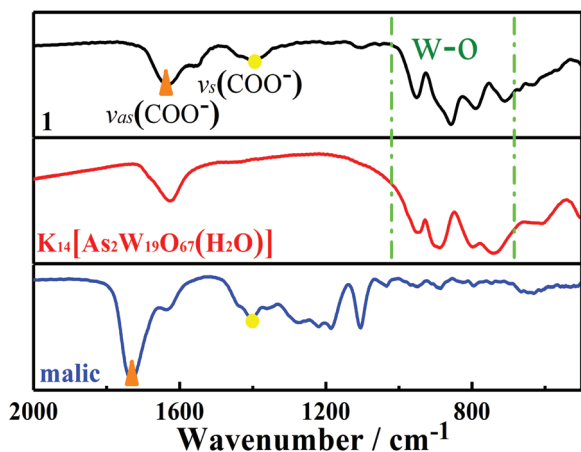


Fig. 2 The IR spectra of **1**, $K_{14}[As_2W_{19}O_{67}(H_2O)]$ precursor, and L-malic acid.

Z represent the stimulus values of the three primary colors); and the generation of multicolor is to blend the three primary colors.²² The color coordinates (x, y) are used to determine the positions of the light sources in the chromaticity diagram. The white light point is also described as equal energy point (x_{ee}, y_{ee}), which is located near the centre of the chromaticity diagram with the standard chromaticity coordinates (0.33, 0.33).²³ Furthermore, the CIE chromaticity coordinates are based on a spectral luminous efficiency function for perceived vision. The dominant wavelength of the illuminant can be seen as the monochromatic color of the light source, and the position of the dominant wavelength could be obtained by the method of drawing a straight line between the white light point coordinates (0.33, 0.33) and the color coordinates, and the line intersects the perimeter of the chromaticity diagram at two intersection points. The spectral color wavelength at the intersection point nearer to the color coordinates can be regarded as the dominant wavelength of the color coordinates (Fig. S5†).²⁴ The theoretical color purity can be calculated by a formula.²⁵ Correlated color temperature (T_{cp} , in kelvin) as a characteristic of visible light has been applied in photography, videography publishing and so on, which is determined by comparing its chromaticity with a theoretical, heated black-body radiator.²⁶

The Pr element in **1** has a +3 charge ($4f^2$ configuration), corresponding to thirteen energy levels (Pr^{3+}), and the ground state is 3H_4 ($4f^2$, produced by the spin-orbit coupling of the 3H state).²⁷ Pr^{3+} ions in **1** demonstrate characteristic intra $4f-4f$ transitions among visible and near-infrared (NIR) ranges with intricate emissions from three different states (3P_0 , 3P_1 and 1D_2) under the excited state.²⁸ The lifetime of the transient PL phenomenon is confirmed and calculated by formulae (1) and (2):²⁹

$$I(t) = \alpha_1 e^{-\frac{t}{\tau_1}} + \alpha_2 e^{-\frac{t}{\tau_2}} \quad (1)$$

$$\tau^* = \frac{\alpha_1 \tau_1^2 + \alpha_2 \tau_2^2}{\alpha_1 \tau_1 + \alpha_2 \tau_2} \quad (2)$$

where α_1 and α_2 are the fractional contributions of decay lifetimes τ_1 and τ_2 , τ_1 represents a short-time component, τ_2 represents a long-time component and τ^* represents average lifetime.

The solid-state sample of **1** emits several characteristic emissions under monitoring the excitation at 450 nm in the visible and NIR areas (Fig. 3a). The mechanism of energy transitions in **1** can be explained that arsenotungstate fragments can be excited from the ground state $^1A_{1g}$ to $^1T_{1u}$ level and subsequently return to the $^3T_{1u}$ level *via* non-radiative transitions. The photoexcitation O \rightarrow M LMCT of arsenotungstate fragments transfers to 4f excited multiplets (such as 3P_1 , 3P_0 and 1D_2) of Pr^{3+} ions with the assistance of intramolecular energy transitions and fast non-radiative transitions in **1**, thereby the excited Pr^{3+} ions emit characteristic visible and NIR emissions. The visible emission spectrum of **1** presents five characteristic peaks at around 530, 607, 621, 646 and 682 nm that are assigned to the $^3P_1 \rightarrow ^3H_5$, $^1D_2 \rightarrow ^3H_4$, $^3P_0 \rightarrow ^3H_6$, $^3P_0 \rightarrow ^3F_2$ and $^3P_1 \rightarrow ^3F_2$ transitions of Pr^{3+} ions, respectively (Fig. 3b). Notably, the $^3P_0 \rightarrow ^3F_2$ transition is stronger than other transitions, which may be due to the intense radiative rate related to the large Judd–Ofelt Ω_2 parameters of the $^3P_0 \rightarrow ^3F_2$ transition that has been mentioned by Cavalli *et al.*³⁰ The PL lifetime of **1** under the conditions of the strongest emission at 646 nm and excitation at 450 nm adheres to a double exponential decay pattern with the values of τ_1 and τ_2 of 1.18 μs (47.47%) and 8.87 μs (52.53%) (the average value of τ^* is 8.04 μs) (Fig. 3c). In addition, the NIR luminescence emission spectrum and lifetime decay curve of the solid-state sample of **1** under the excitation at 450 nm were obtained. The NIR emission spectrum demonstrates two characteristic peaks at 875 and 1042 nm, which are attributed to the $^1D_2 \rightarrow ^3F_2$ and $^1D_2 \rightarrow ^3F_4$ transitions of Pr^{3+} ions, respectively (Fig. 3d). The PL lifetime of **1** showing 1042 nm emission upon 450 nm excitation adheres to a double exponential function. The lifetimes of τ_1 and τ_2 are 0.65 μs (36.73%) and 9.29 μs (63.27%) with the average value of τ^* of 8.95 μs (Fig. 3e). The CIE 1931 chromaticity coordinates of sample **1** based on the corresponding visible PL spectra are (0.47, 0.50), which are located in the orange-yellow area (Fig. S5†). The calculated color purity and correlated color temperature (T_{cp}) of **1** were found to be 92.35% and 3162 K (Fig. S6†). As shown in Fig. S7,† the decay time curves of **1** under the excitation at 450 nm and different emissions at 530, 607, 621, 646 and 682 nm show a similar profile, and all of these curves can be fitted by a double exponential function. The fitting parameters and average PL lifetime τ^* are summarized in Table S3,† showing the similar average fluorescence–decay time. This indicates that the different emission decay times originate from the same excited state (3P_1) when taking no account of non-radiative transitions.³¹

Particularly interesting, **1** features excitation wavelength-dependent emission properties. As shown in Fig. 4a, **1** displays different fluorescence emission signals under different excitation wavelengths from 380 nm to 470 nm. Notably, the emission at around 500 nm is dominant when the excitation wave-

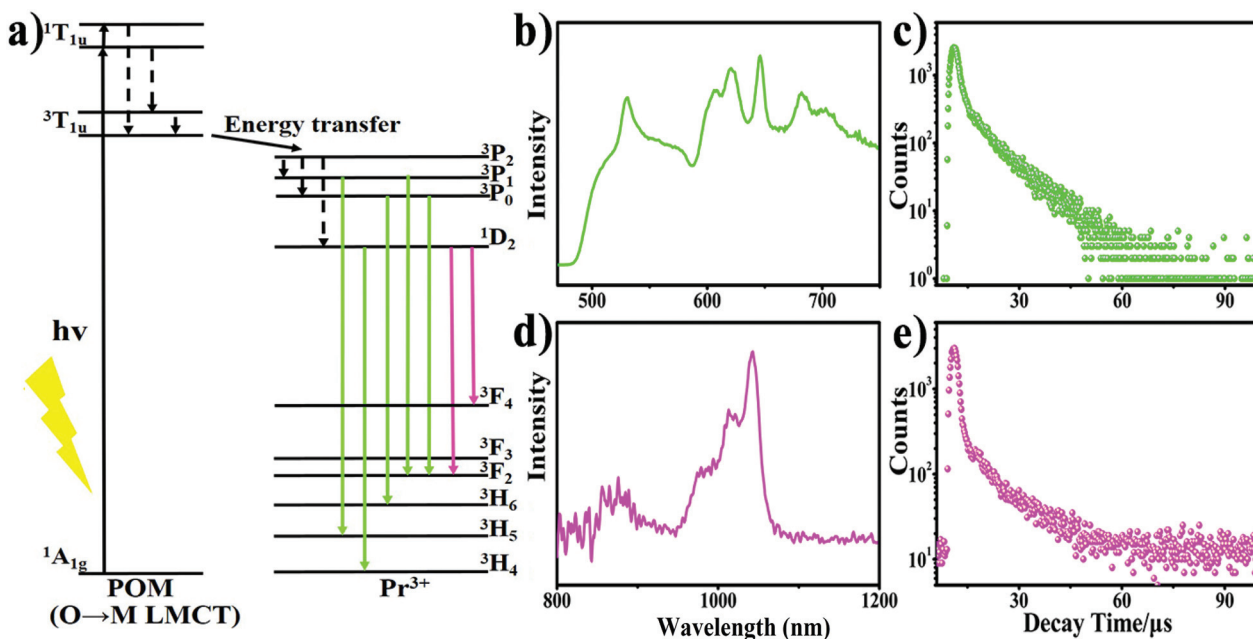


Fig. 3 (a) Visible and NIR luminescence mechanisms for the sensitized emission of Pr^{3+} in complex **1**. (b) The luminescence spectrum of **1** under excitation at 450 nm at room temperature. (c) The decay time curve of **1** under emission at 646 nm at room temperature. (d) The NIR luminescence spectrum of **1** under excitation at 450 nm. (e) The NIR decay time curve of **1** under emission at 1042 nm.

length is less than 430 nm. To explore the origin of the emission at around 500 nm, the emission spectra of the $[\text{As}_2\text{W}_{19}\text{O}_{67}(\text{H}_2\text{O})]^{14-}$ precursor were recorded under different excitation wavelengths from 370 nm to 400 nm, which displays a broad emission signal at approximately 505 nm (Fig. S8[†]). Simultaneously, the excitation spectrum of the $[\text{As}_2\text{W}_{19}\text{O}_{67}(\text{H}_2\text{O})]^{14-}$ precursor was also monitored under emission at 505 nm, which shows two obvious excitation peaks at around 405 and 430 nm (Fig. S9[†]). Apparently, the emission of **1** at around 500 nm under excitation wavelengths from 380 nm to 440 nm may be attributed to the emission of arsenotungstate fragments in **1**. However, the characteristic emissions at 530, 607, 621, 646 and 682 nm of Pr^{3+} ions in **1** become nonnegligible when the excitation wavelength is adjusted from 440 nm to 470 nm under the same conditions. The CIE 1931 chromaticity coordinates vary from the green area (0.32, 0.60) excited at 380 nm to the orange-yellow area (0.49, 0.49) excited at 470 nm, and the correlated color temperature (T_{cp}) declines from 5738 K (cool color) to 2941 K (warm color) (Fig. 4b and Table 1). Besides, we particularly investigated the 3D excitation-dependent PL emission properties under excitation wavelengths from 370 nm to 470 nm (Fig. 4c). It can be found that the emission intensity at 500 nm increases to the maximum under excitation at 495 nm and then gradually decreases. For clarity, the other 3D surface plots from different angles of view are shown in Fig. S10.[†] This interesting phenomenon displays that the PL of **1** can be tuned from green to orange-yellow through the variation of excitation wavelength, and also makes it possible for achieving a reversible

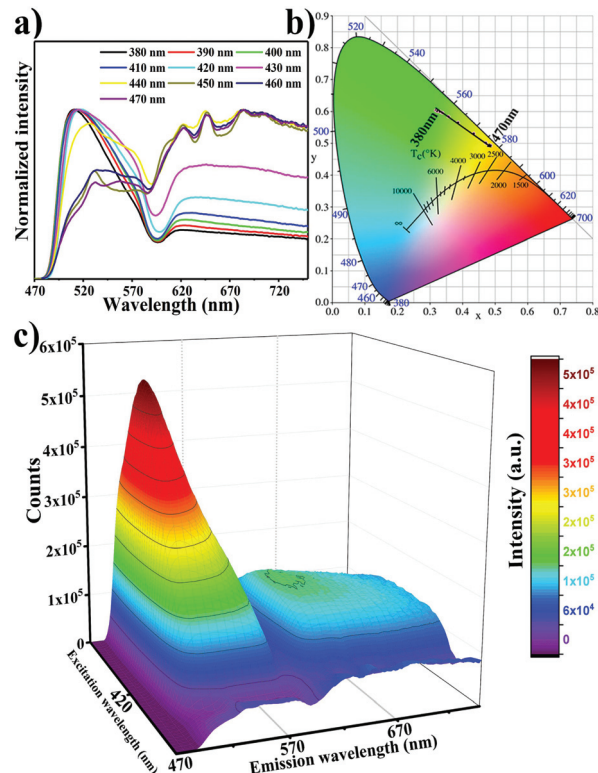


Fig. 4 (a) PL emission spectra of **1** under different excitation wavelengths recorded from 380 nm to 470 nm in 10 nm increments. (b) The CIE 1931 chromaticity coordinates of **1** based on serial excitation wavelengths. (c) The 3D surface plot of the luminescence photoexcitation map.

Table 1 Optical parameters of **1** under different excitation wavelengths recorded from 380 nm to 470 nm

| λ_{ex} (nm) | CIE 1931 coordinates (x, y) | Dominant wavelength (nm) | Color purity (%) | T_{cp} (K) |
|----------------------------|-----------------------------|--------------------------|------------------|---------------------|
| 380 | 0.32, 0.60 | 552 | 78.33 | 5738 |
| 390 | 0.32, 0.60 | 553 | 79.14 | 5662 |
| 400 | 0.33, 0.60 | 554 | 80.29 | 5543 |
| 410 | 0.34, 0.59 | 556 | 82.20 | 5400 |
| 420 | 0.36, 0.58 | 558 | 82.45 | 5103 |
| 430 | 0.39, 0.56 | 563 | 85.84 | 4599 |
| 440 | 0.43, 0.53 | 570 | 89.44 | 3795 |
| 450 | 0.48, 0.49 | 577 | 92.57 | 3001 |
| 460 | 0.47, 0.50 | 576 | 92.35 | 3162 |
| 470 | 0.49, 0.49 | 577 | 94.18 | 2941 |

emission color switching simply *via* changing the excitation wavelength rather than doping of relevant fluorescent dyes.³²

Furthermore, a general methodology of TRES was used to explain the energy transfer process in **1**. Fig. 5a shows the time-resolved emission spectra of **1** under excitation at 450 nm at room temperature. Some meaningful information can be

obtained from the spectral layout. Initially, the obvious emission peak at 500 nm appears at 9.1 μs , and the emission signals at 530, 607, 621, 646 and 682 nm are inconspicuous. After 0.2 μs , the characteristic emission signals of Pr^{3+} ions at 530, 607, 621, 646 and 682 nm are discernible. When the time delay is 10.0 μs , the emission signals of Pr^{3+} ions become dominant, whereas the peak at 500 nm gradually declines to almost invisible. As the time elapsed, the intensity of peaks at 607, 621, 646 and 682 nm gradually increases to a maximum at 15.0 μs , and then it gradually descends. The spectral peak quickly evolves from 500 nm (the emission of arsenotungstate components) to the emission bands at 530, 607, 621, 646 and 682 nm (the emission of Pr^{3+} ions) within ~ 1.0 μs (Fig. 5 and Fig. S12[†]). The results show that the photoexcitation $\text{O} \rightarrow \text{M}$ LMCT of arsenotungstate fragments effectively sensitizes the emission of Pr^{3+} ions *via* intramolecular energy transitions (the antenna effect) in **1**, which provides the observed time-resolved multiple emission bands with complex kinetics. Also, Fig. 5b, Fig. S12 and Fig. S13[†] show another 3D view to intuitively perceive the process of energy transfer.

Conclusions

In summary, we successfully synthesised a 1-D helical chain-like organic-inorganic hybrid arsenotungstate: $\text{Na}_4\text{H}_8[\{\text{Pr}(\text{H}_2\text{O})_2\}_2\{\text{As}_2\text{W}_{19}\text{O}_{68}\}\{\text{WO}_2(\text{mal})\}_2]\cdot 24\text{H}_2\text{O}$ (**1**). The chief role of the malate ligand is that it can construct a five-membered $\text{W}-\text{O}-\text{C}-\text{C}-\text{O}$ chelate ring to stabilize the structure of **1** in this system. The PL of a solid-state sample of **1** under different excitation wavelengths has been systematically studied, revealing that **1** features excitation wavelength-dependent emission behaviours and displays a reversible green-orange-yellow luminescence switching. The TRES of **1** indicates that the photoexcitation $\text{O} \rightarrow \text{M}$ LMCT of arsenotungstate fragments can effectively sensitize the emission of Pr^{3+} ions *via* intramolecular energy transitions. We believe that this work may be beneficial to gain more insight into the POM-based rare earth materials.

Experimental section

Materials and methods

The dilacurary precursor $\text{K}_{14}[\text{As}_2\text{W}_{19}\text{O}_{67}(\text{H}_2\text{O})]$ was synthesized as described and confirmed by IR spectroscopy.³³ Other chemicals were of analytical grade and used as purchased without further purification. Elemental analyses (C and H) were carried out on an Elementar VarioElcubc CHNS analyzer. The TG analysis was performed under a N_2 atmosphere on a NETZSCH STA 449 F5 Jupiter thermal analyzer with the heating rate of 10 $^\circ\text{C min}^{-1}$ from 35 to 1000 $^\circ\text{C}$. IR spectra were recorded in KBr pellets on a Bruker VERTEX 70 IR spectrometer in the range of 400 – 4000 cm^{-1} . The powder X-ray diffraction pattern was recorded on a Bruker D8 ADVANCE instrument with $\text{Cu K}\alpha$ radiation ($\lambda = 1.54056$ \AA).

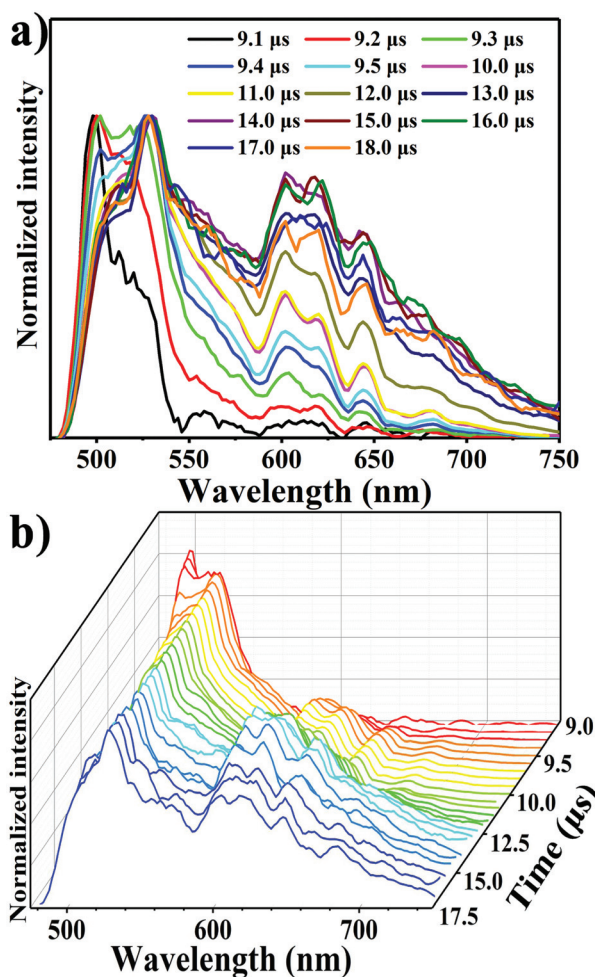


Fig. 5 Reconstructed plots of **1** at room temperature under excitation at 450 nm resolved by microsecond fluorescence: (a) spectral temporal evolution and (b) the 3D time-resolved emission spectrum of **1**.

Photoluminescence and delay time properties were measured on a FL980 fluorescence spectrophotometer.

Synthesis of 1

$K_{14}[As_2W_{19}O_{67}(H_2O)]$ (1.320 g, 0.25 mmol) was dissolved in 40 mL of water, and then L-malic acid (0.134 g, 1.0 mmol), $PrCl_3 \cdot 6H_2O$ (0.223 g, 0.6 mmol) and LiCl (0.850 g, 20.0 mmol) were successively added step by step with stirring at room temperature. After the mixture was stirred for about 10 min, the pH value of the solution was adjusted to approximately 2.8 by the addition of 3 M NaOH solution and then heated to 60 °C for 1.5 h. The resulting mixture was cooled to ambient temperature, clear solution was filtered and left for about two months at ambient temperature to give suitable colorless block crystals for X-ray structure determination. Yield: 33% (based on $K_{14}[As_2W_{19}O_{67}(H_2O)]$). IR (KBr pellet, cm^{-1}): 1633(m), 1399(w), 952(s), 858(s), 790(s), 710(s). Elemental analyses (%) calcd for $Na_4H_8[Pr(H_2O)_2]_2\{As_2W_{19}O_{68}\}\{WO_2(mal)\}_2 \cdot 24H_2O$ (1): C, 1.52; H, 1.12. Found (%): C, 1.58; H, 0.99.

X-ray crystallographic determination

A suitable sample of 1 was collected for the crystallographic study at 296(2) K and intensity data were collected on a Bruker Apex II CCD diffractometer at room temperature with graphite-monochromated Mo $K\alpha$ radiation ($\lambda = 0.71073 \text{ \AA}$). Intensity data were corrected for Lorentz and polarization effects as well as for multi-scan absorption. The structure was solved by direct methods and heavy atoms were located by full-matrix least-squares refinements on F^2 and Fourier syntheses using the SHELXS-1997 program package, which was further refined by full-matrix least squares on F^2 using the SHELXL-2015 program package.³⁴ In the final refinement cycles, all the non-hydrogen atoms were refined anisotropically. The partial lattice water molecules were located by using a Fourier map and the remaining lattice water molecules were determined by TGA results. The hydrogen atoms of the mal

groups and water molecules were placed in calculated positions and then refined using a riding model. Crystallographic data for the structure of 1 have been deposited in the Cambridge Crystallographic Data Center with CCDC number: 1588091 (Table 2).†

Conflicts of interest

There are no conflicts to declare.

Acknowledgements

This work was financially supported by the Natural Science Foundation of Henan Province (132300410144 and 162300410015).

Notes and references

- (a) Q. Dai, M. E. Foley, C. J. Breshike, A. Lita and G. F. Strouse, *J. Am. Chem. Soc.*, 2011, **133**, 15475–15486; (b) R. Gautier, X. Li, Z. Xia and F. Massuyeau, *J. Am. Chem. Soc.*, 2017, **139**, 1436–1439; (c) S. Y. Lee, T. Yasuda, Y. S. Yang, Q. Zhang and C. Adachi, *Angew. Chem., Int. Ed.*, 2014, **53**, 6402–6406; (d) X. Yang, X. Lin, Y. Zhao, Y. S. Zhao and D. Yan, *Angew. Chem., Int. Ed.*, 2017, **129**, 7961–7965; (e) P. Ma, F. Hu, R. Wan, Y. Huo, D. Zhang, J. Niu and J. Wang, *J. Mater. Chem. C*, 2016, **4**, 5424–5433.
- (a) R. Ban, X. Sun, J. Wang, P. Ma, C. Zhang, J. Niu and J. Wang, *Dalton Trans.*, 2017, **46**, 5856–5863; (b) Y. Y. Yeung and P. A. Tanner, *Chem. Phys. Lett.*, 2013, **590**, 46–51; (c) M. Yamada, T. Naitou, K. Izuno, H. Tamaki, Y. Murazaki, M. Kameshima and T. Mukai, *Jpn. J. Appl. Phys.*, 2003, **42**, L20–L23.
- (a) C.-H. Huang, *Rare earth coordination chemistry: fundamentals and applications*, John Wiley & Sons, 2010; (b) L.-M. Li, J.-Q. Ren, G.-X. Xu and X.-Z. Wang, *Int. J. Quantum Chem.*, 1983, **23**, 1305–1316; (c) G.-X. Xu and J.-Q. Ren, *Int. J. Quantum Chem.*, 1986, **29**, 1017–1024; (d) J.-Q. Ren and G.-X. Xu, *Lanthanide Actinide Res.*, 1987, **2**, 67–78.
- (a) N. Mizuno and M. Misono, *Chem. Rev.*, 1998, **98**, 199–217; (b) S. Chen, Y. Liu, J. Guo, P. Li, Z. Huo, P. Ma, J. Niu and J. Wang, *Dalton Trans.*, 2015, **44**, 10152–10155; (c) J. Zhao, J. Wang, J. Zhao, P. Ma, J. Wang and J. Niu, *Dalton Trans.*, 2012, **41**, 5832–5837; (d) A. H. Yang, J. Y. Zou, W. M. Wang, X. Y. Shi, H. L. Gao, J. Z. Cui and B. Zhao, *Inorg. Chem.*, 2014, **53**, 7092–7100.
- (a) P. Ma, R. Wan, Y. Si, F. Hu, Y. Wang, J. Niu and J. Wang, *Dalton Trans.*, 2015, **44**, 11514–11523; (b) C. Ritchie, M. Speldrich, R. W. Gable, L. Sorace, P. Kögerler and C. Boskovic, *Inorg. Chem.*, 2011, **50**, 7004–7014; (c) Y. Wang, P. Ma and J. Niu, *Dalton Trans.*, 2015, **44**, 4679–4682; (d) R. Wan, P. Ma, M. Han, D. Zhang, C. Zhang, J. Niu and J. Wang, *Dalton Trans.*, 2017, **46**, 5398–5405.

Table 2 Crystallographic data and structure refinement parameters for 1

| | 1 |
|---|--------------------------------------|
| Empirical formula | $C_8H_{70}Na_4O_{110}As_2Pr_2W_{21}$ |
| Formula weight | 6310.83 |
| Crystal system | Monoclinic |
| Space group | $C2/c$ |
| a [Å] | 19.802(5) |
| b [Å] | 28.389(8) |
| c [Å] | 21.365(9) |
| β [°] | 109.160(4) |
| V [Å ³] | 11 345(6) |
| Z | 4 |
| ρ_{calcd} [g cm ⁻³] | 3.627 |
| μ [mm ⁻¹] | 22.734 |
| Data/parameters | 10 079/655 |
| R_{int} | 0.0500 |
| GO F | 1.024 |
| R_1, wR_2 [$I > 2\sigma(I)$] | 0.0454, 0.1120 |
| R_1, wR_2 [all data] | 0.0691, 0.1248 |

- 6 (a) H. Zhang, X. Lin, Y. Yan and L. Wu, *Chem. Commun.*, 2006, 4575–4577; (b) C. Ritchie, V. Baslon, E. G. Moore, C. Reber and C. Boskovic, *Inorg. Chem.*, 2012, **51**, 1142–1151; (c) H. Li, W. Qi, H. Sun, W. Bu and L. Wu, *Adv. Mater.*, 2005, **17**, 2688–2692.
- 7 R. D. Peacock and T. J. R. Weakley, *J. Chem. Soc. A*, 1971, 1836–1839.
- 8 M. Sadakane, M. H. Dickman and M. T. Pope, *Angew. Chem., Int. Ed.*, 2000, **39**, 2914–2917.
- 9 P. Mialane, L. Lisnard, A. Mallard, J. Marrot, E. Antic-Fidancev, P. Aschehoug, D. Vivien and F. Sécheresse, *Inorg. Chem.*, 2003, **42**, 2102–2108.
- 10 C. Liu, F. Luo, N. Liu, Y. Cui, X. Wang, E. Wang and J. Chen, *Cryst. Growth Des.*, 2006, **6**, 2658–2660.
- 11 Y. Lu, Y. Xu, Y. Li, E. Wang, X. Xu and Y. Ma, *Inorg. Chem.*, 2006, **45**, 2055–2060.
- 12 A. H. Ismail, M. H. Dickman and U. Kortz, *Inorg. Chem.*, 2009, **48**, 1559–1565.
- 13 C. Ritchie and C. Boskovic, *Cryst. Growth Des.*, 2010, **10**, 488–491.
- 14 J.-Y. Niu, J.-W. Zhao and J.-P. Wang, *Inorg. Chem. Commun.*, 2004, **7**, 876–879.
- 15 J.-P. Wang, X.-Y. Duan, X.-D. Du and J.-Y. Niu, *Cryst. Growth Des.*, 2006, **6**, 2266–2270.
- 16 J.-P. Wang, J.-W. Zhao, X.-Y. Duan and J.-Y. Niu, *Cryst. Growth Des.*, 2006, **2**, 507–513.
- 17 S. Zhang, Y. Wang, J. Zhao, P. Ma, J. Wang and J. Niu, *Dalton Trans.*, 2012, **41**, 3764–3772.
- 18 P. Ma, Y. Si, R. Wan, S. Zhang, J. Wang and J. Niu, *Spectrochim. Acta, Part A*, 2015, **138**, 579–584.
- 19 N. V. Izarova, M. N. Sokolov, D. G. Samsonenko, A. Rothenberger, D. Y. Naumov, D. Fenske and V. P. Fedin, *Eur. J. Inorg. Chem.*, 2005, **24**, 4985–4996.
- 20 (a) C. Ritchie and C. Boskovic, *Cryst. Growth Des.*, 2010, **10**, 488–491; (b) C. Ritchie, C. E. Miller and C. Boskovic, *Dalton Trans.*, 2011, **40**, 12037–12039.
- 21 V. Kulikov, N. A. B. Johnson, A. J. Surman, M. Hutin, S. M. Kelly, M. Hezwani, D. L. Long, G. Meyer and L. Cronin, *Angew. Chem., Int. Ed.*, 2017, **56**, 1141–1146.
- 22 (a) J. E. Kwon, S. Park and S. Y. Park, *J. Am. Chem. Soc.*, 2013, **135**, 11239–11246; (b) S. Shao, J. Ding, L. Wang, X. Jing and F. Wang, *J. Am. Chem. Soc.*, 2012, **134**, 20290–20293; (c) J. K. Jiang, S. Sun, L. Zhang, Y. Lu, A. Wu, C. Cai and H. Lin, *Angew. Chem., Int. Ed.*, 2015, **54**, 5360–5363.
- 23 X. Yan, T. R. Cook, P. Wang, F. Huang and P. J. Stang, *Nat. Chem.*, 2015, **7**, 342–348.
- 24 H. L. Li, J. Y. Liu, J. L. Liu, L. J. Chen, J. W. Zhao and G. Y. Yang, *Chem. – Eur. J.*, 2017, **23**, 2673–2685.
- 25 J. Suresh Kumar, K. Pavani, A. Mohan Babu, N. Kumar Giri, S. B. Rai and L. R. Moorthy, *J. Lumin.*, 2010, **130**, 1916–1923.
- 26 D. B. Judd, D. L. MacAdam, G. Wyszecski, H. W. Budde, H. R. Condit, S. T. Henderson and J. L. Simonds, *J. Opt. Soc. Am.*, 1964, **54**, 1031–1040.
- 27 C. G. Ma, M. G. Brik, D. X. Liu, B. Feng, Y. Tian and A. Suchocki, *J. Lumin.*, 2016, **170**, 369–374.
- 28 S. Dang, J. Yu, X. Wang, L. Sun, R. Deng, J. Feng, W. Fan and H. Zhang, *J. Lumin.*, 2011, **131**, 1857–1863.
- 29 Y. Zhang, J. Zhang, J. Zhang, S. Lin, Y. Huang, R. Yuan, X. Liang and W. Xiang, *Dyes Pigm.*, 2017, **140**, 122–130.
- 30 (a) E. Cavalli, F. Angiuli, P. Boutinaud and R. Mahiou, *J. Solid State Chem.*, 2012, **185**, 136–142; (b) S. Tanabe, T. Hanada, T. Ohyagi and N. Soga, *Phys. Rev. B: Condens. Matter Mater. Phys.*, 1993, **48**, 10591; (c) *Spectroscopic Properties of Rare Earths in Optical Materials*, ed. G. Liu and B. Jacquier, Springer Science & Business Media, 2006, vol. 83.
- 31 E. R. Dohner, E. T. Hoke and H. I. Karunadasa, *J. Am. Chem. Soc.*, 2014, **136**, 1718–1721.
- 32 Q. W. Zhang, D. Li, X. Li, P. B. White, J. Mecinović, X. Ma, H. Ågren, R. J. M. Nolte and H. Tian, *J. Am. Chem. Soc.*, 2016, **138**, 13541–13550.
- 33 A. H. Ismail, B. S. Bassil, I. Römer, N. C. Redeker and U. Kortz, *Z. Naturforsch., B: J. Chem. Sci.*, 2010, **65**, 383–393.
- 34 G. M. Sheldrick, *Acta Crystallogr., Sect. A: Found. Crystallogr.*, 2008, **64**, 112–122.